

Tiltmeter Mapping of Measured Nonsymmetric Hydraulic-Fracture Growth in a Conglomerate/Sandstone Formation Using the Implicit Level-Set Algorithm and the Extended Kalman Filter

V. Pandurangan, CSIRO Energy; A. Peirce, University of British Columbia;
Z. R. Chen, CSIRO Energy; and R. G. Jeffrey, SCT Operations

Summary

A novel method to map asymmetric hydraulic-fracture propagation using tiltmeter measurements is presented. Hydraulic fracturing is primarily used for oil-and-gas well stimulation, and is also applied to precondition rock before mining. The geometry of the developing fracture is often remotely monitored with tiltmeters— instruments that are able to remotely measure the fracture-induced deformations. However, conventional analysis of tiltmeter data is limited to determining the fracture orientation and volume. The objective of this work is to detect asymmetric fracture growth during a hydraulic-fracturing treatment, which will yield height-growth information for vertical fracture growth and horizontal asymmetry for lateral fracture growth or detect low preconditioning-treatment efficiency in mining. The technique proposed here uses the extended Kalman filter (EKF) to assimilate tilt data into a hydraulic-fracture model to track the geometry of the fracture front. The EKF uses the implicit level set algorithm (ILSA) as the dynamic model to locate the boundary of the fracture by solving the coupled fluid-flow/fracture-propagation equations, and uses the Okada half-space solution as the observation model (forward model) to relate the fracture geometry to the measured tilts. The 3D fracture model uses the Okada analytical expressions for the displacements and tilts caused by piecewise constant-displacement discontinuity elements to discretize the fracture area. The proposed technique is first validated by a numerical example in which synthetic tilt data are generated by assuming a confining-stress gradient to generate asymmetric fracture growth. The inversion is carried in a two-step process in which the fracture dip and dip direction are first obtained with an elliptical fracture-forward model, and then the ILSA-EKF model is used to obtain the fracture footprint by fixing the dip and dip direction to the values obtained in the first step. Finally, the ILSA-EKF scheme is used to predict the fracture width and geometry evolution from real field data, which are compared with intersection data obtained by temperature and pressure monitoring in offset boreholes. The results show that the procedure is able to satisfactorily capture fracture growth and asymmetry even though the field data contain significant noise, the tiltmeters are relatively far from the fracture, and the dynamic model contains significant “unmodeled dynamics” such as stress anisotropy, material heterogeneity, fluid leakoff into the formation, and other physical processes that have not been explicitly accounted for in the dynamic ILSA model. However, all the physical processes that affect the tilt signal are incorporated by the EKF when the tilt measurements are used to obtain the maximum likelihood estimates of the fracture widths and geometry.

Introduction

Hydraulic fracturing has been used for oil-and-gas well stimulation since the late 1940s (Montgomery and Smith 2010), and is also used as a preconditioning method to promote earlier and more-continuous caving in underground coal and metal mines (Jeffrey et al. 2013). The goal of hydraulic-fracture design is to optimize the treatment such that a fracture length and fracture conductivity are achieved that maximize productivity while minimizing cost. Hence, information about the fracture geometry and fracture height, width, and orientation is required to study the efficacy of a fracturing treatment and to further optimize future treatments.

Most conventional hydraulic-fracture design models assume symmetric/lateral fracture growth about the wellbore. In real treatments, the fracture growth can be asymmetric. Asymmetric fracture geometry develops when the fracture grows preferentially in one direction with respect to the wellbore. In the case of vertical fractures, asymmetric fracture growth may develop with unequal lateral growth or unequal vertical growth or both. Unequal vertical growth is common because the vertical growth occurs through rock layers with contrasting properties and containing contrasting confining stresses. Such vertical growth or height growth not only leads to a less effective stimulation but can also result in the fracture growing into water-bearing formations that may be affected by the treatment or by the later production of the well. Asymmetric growth is often associated with reduced fracture conductivity over the pay zone, and may also lead to a proppant screenout, further reducing the effectiveness of the fracturing treatment (Bennett et al. 1983; Jeffrey 1996). Asymmetry in the lateral growth of a fracture is attributed to interaction with adjacent, previously placed hydraulic fractures that impose an additional compressive stress in the reservoir rock around the fracture. A new fracture will then tend to avoid these more highly stressed areas, leading to asymmetric growth and less-complete stimulation of the reservoir. Because the fracture asymmetry can have a significant effect on the effectiveness and efficiency of a hydraulic-fracturing treatment, it is useful to have methods to monitor asymmetric fracture growth.

Fracture-monitoring techniques map hydraulic-fracture geometry indirectly with remote-monitoring methods applied at the wellsite, which provides helpful guidance for controlling the treatment and for optimization of future hydraulic-fracturing designs. Microseismic-event location and tilt measurements are two commonly used techniques to monitor fracture growth. Tiltmeters are instruments that can measure small rotational movements with respect to the gravity vector along two orthogonal directions. The opening and shearing of the hydraulic-fracture surfaces result in rock deformations, which, in turn, cause small rotational movements at the tiltmeter location. The induced movements are picked up by these instruments located either close to the surface

the state vector \mathbf{x}_k and the error covariance Γ_k at the time \mathbf{t}_k are projected forward in time using the dynamic model:

$$\begin{aligned}\hat{\mathbf{X}}_{k+1|k} &= \mathbf{f}_k(\hat{\mathbf{X}}_{k|k}) \\ \Gamma_{k+1|k} &= \mathbf{F}_k \Gamma_{k|k} \mathbf{F}_k^T + \Gamma_{qk} \dots \dots \dots (2)\end{aligned}$$

Because the dynamic model $\mathbf{f}_k(\cdot)$ is nonlinear, the Jacobian \mathbf{F}_k is used to linearize the covariance estimate about the predicted state, and is defined as

$$\mathbf{F}_k = \frac{\partial \mathbf{f}_k(\hat{\mathbf{X}}_{k|k})}{\partial \mathbf{x}} \dots \dots \dots (3)$$

In the correction step or measurement update, the predictions are updated by adding a weighted difference between the actual and predicted measurements. The weighting factor, known as the Kalman gain \mathbf{K}_{k+1} , minimizes the posteriori-error covariance:

$$\begin{aligned}\mathbf{K}_{k+1} &= \Gamma_{k+1|k} \mathbf{H}_{k+1}^T (\mathbf{H}_{k+1} \Gamma_{k+1|k} \mathbf{H}_{k+1}^T + \Gamma_{v_{k+1}})^{-1} \\ \hat{\mathbf{X}}_{k+1|k+1} &= \hat{\mathbf{X}}_{k+1|k} + \mathbf{K}_{k+1} [\mathbf{y}_{k+1} - \mathbf{H}_{k+1}(\hat{\mathbf{X}}_{k+1|k})] \\ \Gamma_{k+1|k+1} &= (\mathbf{I} - \mathbf{K}_{k+1} \mathbf{H}_{k+1}) \Gamma_{k+1|k} \dots \dots \dots (4)\end{aligned}$$

The following set of scaling parameters is introduced to deal with the small magnitude of the tilt measurements:

$$\begin{aligned}\boldsymbol{\varepsilon} &= \|\mathbf{H}_1\|_2, \\ \mathbf{H}_k &= \boldsymbol{\varepsilon} \mathcal{H}_k, \mathbf{y}_k = \boldsymbol{\varepsilon} \mathcal{Y}_k, \Gamma_{ij} = \boldsymbol{\sigma}_q^2 \mathcal{G}_{ij}, \gamma := \boldsymbol{\sigma}_v^2 / \boldsymbol{\sigma}_q^2 \boldsymbol{\varepsilon}^2, \dots \dots (5)\end{aligned}$$

where \mathcal{H}_k is the scaled Green's function operator. The Kalman gain and the measurement update equations can then be expressed in terms of the scaled variables as follows:

$$\mathbf{K}_{k+1} = \boldsymbol{\varepsilon}^{-1} \mathcal{K}_{k+1},$$

where

$$\begin{aligned}\mathcal{K}_{k+1} &= \mathcal{G}_{k+1|k} \mathcal{H}_{k+1}^T (\mathcal{H}_{k+1} \mathcal{G}_{k+1|k} \mathcal{H}_{k+1}^T + \gamma \mathbf{I})^{-1} \\ \hat{\mathbf{x}}_{k+1|k+1} &= \hat{\mathbf{x}}_{k+1|k} + \mathcal{K}_{k+1} (\mathcal{Y}_{k+1} - \mathcal{H}_{k+1} \hat{\mathbf{x}}_{k+1|k}), \dots \dots \dots (6)\end{aligned}$$

where \mathcal{K}_{k+1} is the scaled Kalman gain matrix. The scaling parameter, γ introduced previously in Eq. 5, provides a rationale for selecting the prior process and measurement-noise covariance. A larger value of γ implies a smaller value of Kalman gain, meaning that the filter gives more weighting (or confidence) to the dynamic model in arriving at the predictions. Hence, to assimilate tilt data into the models, it would be useful to work with smaller values of $\gamma = \Phi^2$, where $\boldsymbol{\sigma}_v = \Phi \boldsymbol{\sigma}_w \boldsymbol{\varepsilon}^2$. The parameter Φ can be adjusted to reflect the resolution of the measurements relative to the fidelity of the dynamic model. The parameter Φ can therefore be used to adjust the way in which the ILSA-EKF algorithm weights the dynamic forward model relative to the tilt measurements. It is typically assigned a value in the range $0.01 < \Phi < 2$ (Peirce and Rochinha 2012). The smaller values $0.01 < \Phi < 0.5$ are appropriate when the measured data have a higher signal-noise ratio and the dynamic forward model does not fully capture the physics of the problem, and larger values $0.5 < \Phi < 2$ when the measurements are significantly noisier (Peirce and Rochinha 2012).

Though using higher values of Φ can be useful when dealing with noisy data, it also lowers the Kalman gain, meaning that the measurements contribute little toward improving the model estimates.

Dynamic Model ILSA. The ILSA scheme (Peirce and Detournay 2008) is a numerical technique to locate the boundary of a propagating hydraulic fracture. As with any hydraulic-fracture model, the ILSA model is built on three main components: the elasticity equation relating the net pressure in the fracture to the elastic fracture opening, the fluid-flow equation that governs the pressure drop within the fracture consistent with mass conservation, and the fracture front-propagation condition. The novelty of the ILSA scheme is that it uses a tip asymptotic relationship, valid for a given propagation regime, in combination with an implicit algorithm that is based on a level-set method to track the position

of the fracture front. The method is briefly presented in this section for completeness. The detailed formulation of the method can be found in Peirce and Detournay (2008).

First, the elasticity equation relates the fracture width $\mathbf{w}(\mathbf{x}, \mathbf{y}, \mathbf{t})$ and the fluid pressure \mathbf{p}_f within the fracture. For a planar fracture in an infinite homogeneous medium occupying a region \mathcal{S} at any time \mathbf{t} , the integral equation that relates \mathbf{p}_f to \mathbf{w} is as follows:

$$\begin{aligned}\mathbf{p} &= \mathbf{p}_f(\mathbf{x}, \mathbf{y}, \mathbf{t}) - \boldsymbol{\sigma}_0(\mathbf{x}, \mathbf{y}) \\ &= -\frac{\mathbf{E}'}{8\pi} \int_{\mathcal{S}(\mathbf{t})} \frac{\mathbf{w}(\mathbf{x}', \mathbf{y}', \mathbf{t}) d\mathcal{S}(\mathbf{x}', \mathbf{y}')}{[(\mathbf{x}' - \mathbf{x})^2 + (\mathbf{y}' - \mathbf{y})^2]^{3/2}}, \dots \dots \dots (7)\end{aligned}$$

where $\mathbf{E}' = \frac{\mathbf{E}}{1 - \nu^2}$ is the plane-strain modulus and \mathbf{p} the net pressure or the pressure in excess of the far-field confining stress (minimum principal stress) $\boldsymbol{\sigma}_0$. Because hydraulic fractures are predominantly opening-mode fractures, the fracture width is always taken to be positive.

Second, the Reynolds lubrication equation, describing fluid flow within the fracture, is obtained by combining Poiseuille's law, which relates the fluid flux to the pressure drop within the fracture, with the conservation of mass which implies that any injected fluid stays within the fracture plane:

$$\frac{\partial \mathbf{w}}{\partial \mathbf{t}} = \frac{1}{\boldsymbol{\mu}'} \nabla \cdot (\mathbf{w}^3 \nabla \mathbf{p}_f) + \boldsymbol{\delta}(\mathbf{x}, \mathbf{y}) \mathbf{Q}(\mathbf{t}) \dots \dots \dots (8)$$

Here, $\boldsymbol{\mu}' = 12\boldsymbol{\mu}$ is the scaled fluid viscosity, $\mathbf{Q}(\mathbf{t})$ is the fluid-injection rate, and $\boldsymbol{\delta}(\mathbf{x}, \mathbf{y})$ is the Dirac delta function. The coupled Eqs. 7 and 8 are solved by assuming a zero-flux boundary condition along the fracture front, and that the fluid completely fills the fracture and there is no fluid lag at the tip; that is, by assigning

$$\lim_{\xi \rightarrow 0} \mathbf{w}^3 \frac{\partial \mathbf{p}_f}{\partial \xi} = 0. \dots \dots \dots (9)$$

The energy required for propagating the fracture is primarily supplied by the fluid pressure applied to the injected fluid, which is dissipated during the propagation process. The dissipation phenomenon is mainly governed by viscous losses as the fluid flows through the fracture and the breakage of rock at the fracture tip, each of which is associated with a characteristic length scale. This results in a multiscale solution that is dependent on the propagation regime (Peirce 2015). For hydraulic-fracturing treatments carried out under field conditions, the fracture propagation is dominated by viscous dissipation (Adachi et al. 2007). Therefore, in the present study, we consider the propagation to be in the viscosity-dominated regime without leakoff, in which case the tip asymptotic relationship is of the form

$$\lim_{\xi \rightarrow \infty} \mathbf{w} \sim \boldsymbol{\beta}_{m0} \left(\frac{\boldsymbol{\mu}' \mathbf{v}}{\mathbf{E}'} \right)^{1/3} \xi^{2/3}, \dots \dots \dots (10)$$

where $\boldsymbol{\beta}_{m0} = 2^{1/3} 3^{5/6}$, \mathbf{v} is the fluid tip velocity, and ξ is the distance to the fracture perimeter. The tip asymptotic relation provides the necessary information for determining the position of the fracture front.

To solve the coupled Eqs. 7 and 8 numerically, the fracture boundary $\mathcal{S}(\tau)$ is assumed to grow within a rectangular region discretized with uniform rectangular elements. With piecewise-constant DD elements, and the collocation technique, the elasticity Eq. 7 can be converted to a set of algebraic equations that can be written in a matrix form as

$$\mathbf{p} = \mathbf{C} \mathbf{w}, \dots \dots \dots (11)$$

where the matrix elements are given as

$$\mathbf{C}_{k-m, l-n} = -\frac{\mathbf{E}'}{8\pi} \left[\frac{\sqrt{(\chi_k - \chi_l)^2 + (\zeta_l - \zeta_k)^2}}{(\chi_k - \chi_l)(\zeta_l - \zeta_k)} \right]_{\chi = \chi_m + \frac{\Delta \chi}{2}, \zeta = \zeta_n + \frac{\Delta \zeta}{2}}^{\chi = \chi_m + \frac{\Delta \chi}{2}, \zeta = \zeta_n - \frac{\Delta \zeta}{2}} \dots \dots \dots (12)$$

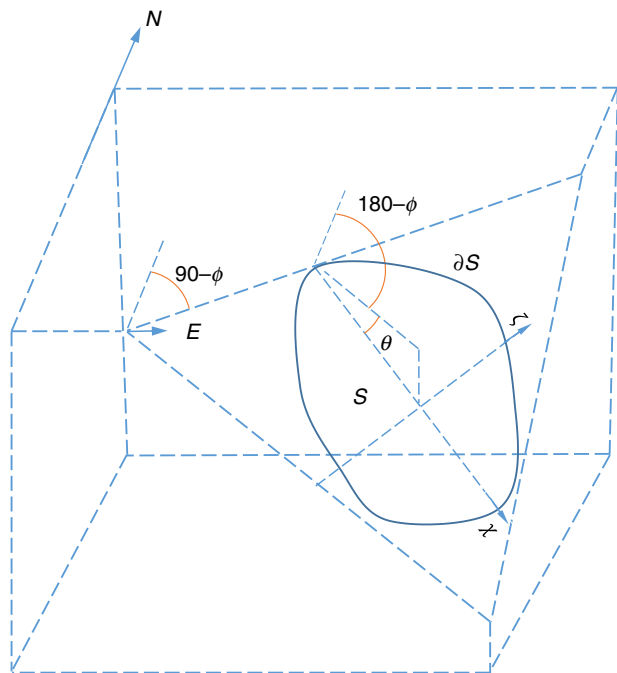


Fig. 1—Fracture parameters of the ILSA-EKF model. The dip, strike, and dip direction are indicated as θ , $90^\circ - \phi$, and $180^\circ - \phi$, respectively.

The fluid flow Eq. 8 is spatially discretized by a central-difference scheme, with the pressure \mathbf{p} and fracture width \mathbf{w} taken at the element centers. After substituting for pressure from Eq. 11, the coupled fluid-flow–elasticity equation can be expressed in a discrete form as

$$\mathbf{w}(\mathbf{t} + \Delta\mathbf{t}) - \mathbf{w}(\mathbf{t}) = \Delta\mathbf{t}\mathbf{A}[\mathbf{w}(\mathbf{t} + \Delta\mathbf{t})]\mathbf{C}\mathbf{w}(\mathbf{t} + \Delta\mathbf{t}) + \Delta\mathbf{t}\mathbf{s}(\mathbf{t} + \Delta\mathbf{t}), \quad \dots \dots \dots (13)$$

where $\mathbf{A}(\mathbf{w})$ is the central-difference operator obtained by spatial discretization of Eq. 8, and $\mathbf{s}(\mathbf{t})$ corresponds to the source term at the wellbore. Because the discretized Eq. 13 is very stiff, the L-stable backward Euler scheme is used for marching the solution forward in time.

The location of the fracture perimeter at any time $(\mathbf{t} + \Delta\mathbf{t})$ is determined with the level-set method. In this method, the fracture contour \mathcal{S} is implicitly represented as the zeroth level set $\mathbf{T}(\mathbf{x}, \mathbf{y}, \mathbf{t}) = 0$ of a surface $\mathbf{Z} = \mathbf{T}(\mathbf{x}, \mathbf{y}, \mathbf{t})$ with $\mathbf{T} < 0$ corresponding to points inside the fracture boundary and vice-versa. Starting with an initial guess of the fracture footprint, the coupled Eq. 13 is solved to obtain the fracture width closest to the fracture boundary. Assuming that the fracture propagation is in the viscous regime, the asymptotic solution (Eq. 10) is inverted to obtain the distance from reference points within the fracture to the fracture boundary:

$$\mathbf{T}(\mathbf{x}, \mathbf{y}, \mathbf{t}) = -\xi \approx - \left[\frac{\mathbf{w}}{\beta_{m0}} \left(\frac{\mathbf{E}'}{\mu' \nu} \right)^{1/3} \right]^{3/2} \text{ for all } (\mathbf{x}, \mathbf{y}) \in \partial\mathcal{S}^c. \quad \dots \dots \dots (14)$$

The frontal velocity is approximated by a finite-difference quotient involving the signed distance functions at two successive timesteps, resulting in a cubic equation that can be solved to obtain the signed distance function $\mathbf{T}(\mathbf{x}, \mathbf{y}, \mathbf{t} + \Delta\mathbf{t})$. Using these boundary values obtained from the solution of the cubic that results from eliminating \mathbf{v} from Eq. 15, the neighboring values of the signed-distance function are obtained by solving the Eikonal equation,

$$|\nabla\mathbf{T}(\mathbf{x}, \mathbf{y}, \mathbf{t} + \Delta\mathbf{t})| = 1. \quad \dots \dots \dots (15)$$

Thus, by evolving the signed-distance surface $\mathbf{Z} = \mathbf{T}(\mathbf{x}, \mathbf{y}, \mathbf{t} + \Delta\mathbf{t})$, we can identify the fracture perimeter as the zero level-set curve $\mathbf{T}(\mathbf{x}, \mathbf{y}, \mathbf{t} + \Delta\mathbf{t}) = 0$.

Forward-Observation-Model–Displacement-Discontinuity Method. Rock deformation associated with hydraulic-fracture growth induces deformations and tilts at the tiltmeter locations, and a forward-observation model is required to relate these deformations and tilts to the generated fracture geometry. The DD technique has been mainly used to construct 3D fracture models such as the solution for the displacement and tilt caused by point displacement discontinuities or rectangular fractures with a constant or variable opening in an elastic half-space or full space (Davis 1983; Yang and Davis 1986; Okada 1992; Olson et al. 1997). An elastic half-space model, as shown in Fig. 1, is useful for analyzing data from a surface-tiltmeter array.

The displacements \mathbf{u}_i at any point \mathbf{x} in the medium, caused by a DD singularity at the point \mathbf{x}' , can be obtained using the principle of superposition as

$$\mathbf{u}_i(\mathbf{x}) = \int_{\mathcal{S}} [\mathbf{U}_{ijk}(\mathbf{x}, \mathbf{x}')\mathbf{n}_j\mathbf{n}_k\mathbf{D}_n(\mathbf{x}') + \mathbf{U}_{ijk}(\mathbf{x}, \mathbf{x}')\mathbf{s}_j\mathbf{n}_k\mathbf{D}_s(\mathbf{x}')]\mathbf{d}\mathbf{s} \quad (i, j, k = 1, 2, 3), \quad \dots \dots \dots (16)$$

where $\mathbf{U}_{ijk}(\mathbf{x}, \mathbf{x}')$ is the displacement vector that represents the fundamental solution. $\mathbf{D}_n = \mathbf{D}_{ij}\mathbf{n}_i\mathbf{n}_j$ and $\mathbf{D}_s = \mathbf{D}_{ij}\mathbf{s}_i\mathbf{n}_j$ correspond to the normal and shear components of the DD vector, respectively. The previous integral is singular when $\mathbf{x} = \mathbf{x}'$, but this issue is easily resolved in the case of tiltmeter mapping because the measurement points \mathbf{x} are always outside the fracture plane. In the DD method, the fracture plane is discretized with piecewise-constant rectangular DD elements. Here, we consider a planar fracture over the surface \mathcal{S} , with a unit normal \mathbf{n} and unit vector \mathbf{s} along the fracture plane, and discretize it with rectangular elements, each with a constant DD field. For these rectangular constant-strength DD elements, Eq. 16 can be integrated analytically. In this work, we have used the analytical expression for the internal deformation and strains caused by a rectangular DD in an elastic half-space developed by Okada (1992). The Okada solution provides simplified closed-form expressions for an arbitrarily oriented shear or tensile fracture in an elastic half-space. The rectangular elements, used to discretize the governing Eqs. 7 and 8, can also be used as the rectangular DD elements of the Okada model.

Because hydraulic fractures are predominantly opening-mode fractures, only the normal component of the DD is considered in this study. At a given tiltmeter location, the tiltmeter measures rotation movements along two orthogonal directions ω_1 and ω_2 with reference to the gravity vector that can be related to the curl of the displacement vector as

$$\omega_1 = \mathbf{u}_{3,1} - \mathbf{u}_{1,3}; \quad \omega_2 = \mathbf{u}_{3,2} - \mathbf{u}_{2,3}, \quad \dots \dots \dots (17)$$

where the comma denotes the derivative with respect to the second index. If the tiltmeters are set up on a free surface and used like a typical carpenter’s level, the tilt data can be related to the horizontal component of the vertical displacement alone, and we have $\omega_1 = -u_{3,1}$ and $\omega_2 = -u_{3,2}$. However, for monitoring hydraulic-fracture growth, tiltmeters are often installed in shallow boreholes and are fully coupled to the rock mass. For an isotropic elastic medium, the stresses σ_{13} and σ_{23} vanish close to a free surface, meaning that $u_{3,1} = -u_{1,3}$ and $u_{2,3} = -u_{3,2}$. In this case, the two modes of deformation—the difference of horizontal displacement as well as the difference of vertical displacement between the endpoints of the instrument—induce tilt, and we have $\omega_1 = -2u_{3,1}$ and $\omega_2 = -2u_{3,2}$. If this factor of 2 is not taken into account and the tilt data are analyzed with $\omega_1 = -u_{3,1}$ and $\omega_2 = -u_{3,2}$, it can result in an estimated fracture volume that is twice the actual fracture volume. This can, in some cases, cause the estimated treatment efficiency, which is the ratio of the

fracture volume to the injected fluid volume, to increase beyond 100% which is physically not possible (Lecampion et al. 2005b).

ILSA-EKF Algorithm. With the ILSA framework and the observation model defined, this section describes the algorithmic steps in the assimilation process. The first step is to identify the state variables for the EKF. Referring to Fig. 1, the possible choices are the fracture geometry $\partial\mathcal{S}$, fracture width \mathbf{w} , the fracture dip θ , and dip direction $180 - \phi$. However, in the current paper, only the fracture widths \mathbf{w}_{mn} for every rectangular element $\Delta\mathcal{S}_{mn}$ over the fracture domain are chosen as the state variables. It is possible to parameterize and include the fracture geometry or the fracture boundary as additional state variables in the EKF, instead of estimating them from the ILSA model. However, this approach does not give satisfactory results because, in a majority of cases, the tiltmeter measurements are in the far-field regime (Lecampion et al. 2005a), meaning that the distance between the tiltmeter location and the fracture plane is much greater (roughly three times) than the characteristic dimension of the fracture. Under such conditions, the fracture width and the geometry are strongly correlated, making it difficult to uniquely recover them by inverting tilt data (Lecampion et al. 2005a; Pandurangan et al. 2015). Including the dip and dip direction as state variables is also not possible because the current ILSA model assumes the fracture to be planar, and predicts the evolution of the fracture boundary at any time \mathbf{t} on the basis of the assumption that dip and dip direction are held constant. If the dip and dip direction are included as additional state variables, their values will change with every timestep, making the ILSA predictions invalid. Therefore, in the current algorithm, the dip and dip direction are obtained with an elliptical fracture-forward model (thus, referred to as the TAL-tilt analysis library) (Lecampion and Gunning 2007; Pandurangan et al. 2015), in the preliminary analysis step, and are fixed during the simulation step with the ILSA-EKF algorithm.

In the prediction update step, the fracture widths $\hat{\mathbf{w}}_{k+1|k}$ at time \mathbf{t}_{k+1} are obtained by solving the coupled Eq. 13, by fixing the fracture front $\partial\mathcal{S}_k$ at timestep \mathbf{t}_k . To begin with, the fracture front is assumed to be radial. In the update step, all tilt data up to time \mathbf{t}_{k+1} are assimilated to obtain a corrected estimate of the fracture widths $\hat{\mathbf{w}}_{k+1|k+1}$. In case the corrected fracture widths are negative, which is physically not possible, they are reset to the predicted estimates. Because the predicted values are obtained from the converged solution to the coupled Eq. 13, they are all positive. The ILSA algorithm is then used to obtain the new front position $\partial\mathcal{S}_{k+1}$ with the corrected estimates of the fracture widths. This procedure is repeated until the front positions have converged within a given timestep. The algorithmic steps in the ILSA-EKF scheme are summarized next. Superscripts are used to distinguish front iterations from timesteps. For example, $\hat{\mathbf{w}}_{k+1|k}^j$ refers to the predicted fracture width during the j th front iteration within the $(k+1)$ th timestep.

1. Set the fracture boundary to be the circle $\mathcal{S}_1 = [(\chi, \zeta) : \sqrt{(\chi - \chi_c)^2 + (\zeta - \zeta_c)^2} \leq \rho_{\text{exact}}(\tau_1)]$.
2. Initialize the EKF parameters Φ and the initial covariance matrix $\Gamma_{1|1} = \sigma_q^2 \mathbf{I}$.
3. Do for N_t timesteps:
 - a. Advance the timestep $\mathbf{t}_{k+1} = \mathbf{t}_k + \Delta t$.
 - b. Fix the fracture front and error covariance from the previous timestep $\partial\mathcal{S}_{k+1}^1 = \partial\mathcal{S}_k$; $\Gamma_{k|k}^1 = \Gamma_{k|k}$.
 - c. Do for N_j front iterations:
 - i. Given $\hat{\mathbf{w}}_{k|k}^j$ and $\partial\mathcal{S}_{k+1}^j$, solve the coupled Eq. 13 to predict $\hat{\mathbf{w}}_{k+1|k}^j$.
 - ii. Compute the Jacobian \mathbf{F}_k^j using Eq. 3.
 - iii. Predict the error-covariance matrix $\Gamma_{k+1|k}^j$ with Eq. 2.
 - iv. Calculate the Kalman gain $\mathbf{K}_{k+1|k}^j$ and the corrected widths $\hat{\mathbf{w}}_{k+1|k+1}^{j+1}$.
 - v. Set $\hat{\mathbf{w}}_{k+1|k+1}^{j+1} = \hat{\mathbf{w}}_{k+1|k}^{j+1}$ for elements for which the corrected width is negative.
 - vi. Update the posterior error covariance $\Gamma_{k+1|k+1}^{j+1}$ with Eq. 4.

- vii. Use the corrected widths and the level-set algorithm (Eqs. 14 and 15) to obtain the new front position

$$\partial\mathcal{S}_{k+1|k+1}^{j+1}$$

- c. End of front iteration.
4. End of timestep loop.

The EKF formulation used in this paper is based on the linearization of the governing equations that does not necessarily preserve the variance and covariance of the full dynamical system, but rather imposes the Gaussian variance and covariance inherited from the linearized system. However, when the model is highly nonlinear, this linear approximation can lead to a suboptimal and biased solution, and the covariance update may not be exact. The EKF also requires the Jacobian matrix for propagating the error covariance, which is computationally expensive. Particle-based approaches such as the ensemble KF (EnKF) and the unscented Kalman filter (UKF), in contrast, use a strategically chosen “ensemble” of trajectories to evaluate the variance and covariance numerically. The error covariance is thus obtained as an ensemble estimate instead of the linear approximation used in the EKF. The EnKF makes use of Monte Carlo sampling to select the ensemble members whereas, in the case of the UKF, the ensemble members, also known as sigma points, are chosen deterministically. Although particle-based approaches can be more efficient than the EKF and are better suited for highly nonlinear models, for the coupled hydraulic-fracturing problem presented in this paper, this would involve a solution to the coupled system of Eq. 13 at every sample point. This would be computationally very demanding and clearly requires more development. This is beyond the scope of the current paper but is certainly an avenue for further investigation.

Numerical Experiment

Synthetic Example. The robustness of the ILSA-EKF algorithm has been demonstrated for 1D and 2D cases with the infinite-space observation model in earlier studies (Peirce and Rochinha 2012) by use of synthetic data sets, under both near-field and far-field regimes. Therefore, the purpose of the numerical example presented here is to demonstrate the performance of the ILSA-EKF algorithm updated with the half-space observation model. Near- and far-field measurements are differentiated on the basis of a term known as the resolution index given by the ratio of the distance \mathbf{d} between the tiltmeter and the fracture plane and the characteristic half-length \mathbf{l} of the fracture. Measurements are considered to be in the far field if this ratio is greater than three (Lecampion et al. 2005a).

Synthetic data were generated by considering a fracture that is initially penny-shaped and growing in a homogeneous elastic half-space, with the injection point 50 m below the surface. The fracture orientation defined by the dip and dip direction is assumed to be 30° and 20° , respectively. Further, the fracture is assumed to propagate in the viscosity-dominated regime, and to be subject to a linearly varying confining-stress field $\sigma_0(\mathbf{x}, \mathbf{y})$ of the form

$$\sigma_0(\chi, \zeta) = \frac{\chi_M - \chi}{\chi_M - \chi_m}, \dots \dots \dots (18)$$

where χ_m and χ_M refer to the minimum and maximum χ coordinates of the rectangular mesh, respectively. Hydraulic fractures tend to grow from high-stress toward low-stress zones because less energy is required to extend a fracture into the low-stress zone (Wu et al. 2008). Therefore, the linearly decreasing confining-stress field (Eq. 18) with linearly increasing χ causes asymmetric fracture growth in the χ direction. For the observation model, we assume a surface-tiltmeter array, as shown in Fig. 2, with coordinates defined as

$$\chi = \zeta = \{7.25 : 10 : 57.25\}, \quad \eta = 10, \dots \dots \dots (19)$$

where η is the depth at which the tiltmeter array is located. The \mathbf{x} and \mathbf{y} components of the tilt vector are measured at every tiltmeter location for 100 discrete timesteps, generating a time-series. To

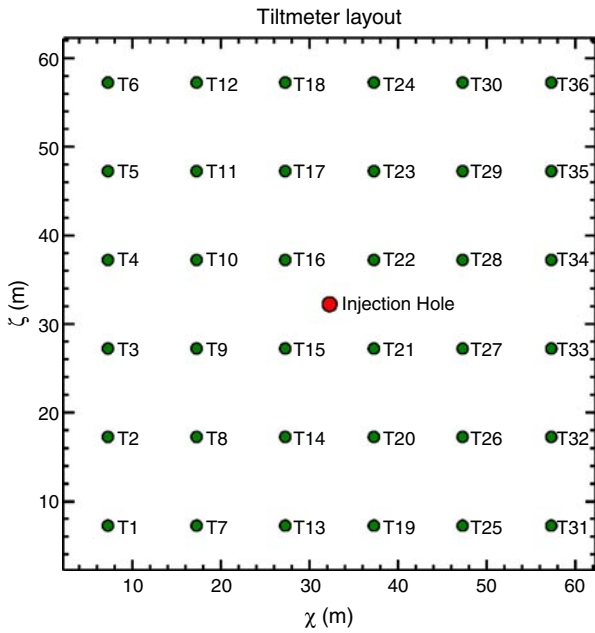


Fig. 2—Tiltmeter layout used for generating the synthetic data set.

simulate field conditions, a zero-mean Gaussian noise with variance σ_N^2 in the range 0–8% is added to the generated tilt measurements. The ILSA-EKF algorithm previously discussed is then used to predict the fracture footprint from these noisy data. In the simulation, the dynamic forward model assumes no confining stress $\sigma_0 = 0$. This implies that the ILSA model would predict radially symmetric fractures in the absence of feedback from the tilt data. The performance of the ILSA-EKF scheme is evaluated with the following error measures:

$$\mathcal{E}_W(\mathbf{t}_k; \phi, \sigma_N) := \frac{\int_{S_k^s \cup S_k^{E-1}} |w^s(\chi, \zeta, \mathbf{t}_k) - w^{E-1}(\chi, \zeta, \mathbf{t}_k)| dS}{\int_{S_k^s} |w^s(\chi, \zeta, \mathbf{t}_k)| dS} \dots \dots \dots (20)$$

$$\mathcal{E}_F(\mathbf{t}_k; \phi, \sigma_N) := \frac{\mathcal{A}[(S_k^s \cup S_k^{E-1}) \setminus (S_k^s \cap S_k^{E-1})]}{\mathcal{A}[S_k^s]} \dots \dots \dots (21)$$

Here, $\mathcal{E}_W(\mathbf{t}_k)$ is the width error that measures the relative difference between the actual (synthetic) and estimated fracture widths at time \mathbf{t}_k , $\mathcal{E}_F(\mathbf{t}_k)$ is the footprint error that measures the relative difference between the actual and estimated fracture geometries,

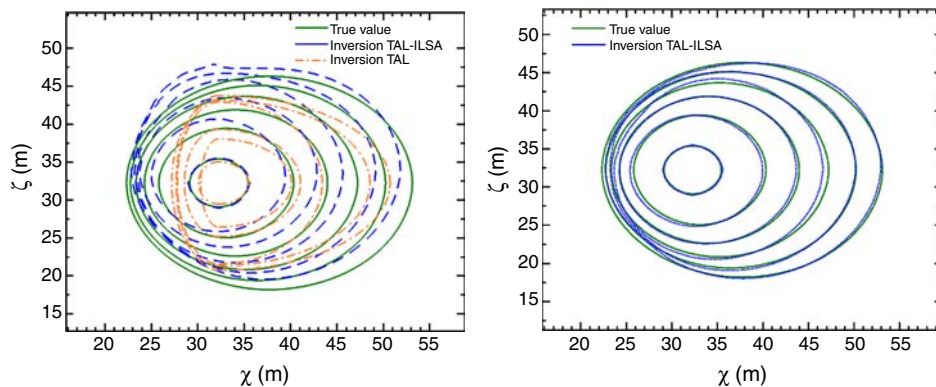


Fig. 3—Left figure: Comparison of synthetic front (solid lines) with ILSA-EKF front (dotted lines) and TAL front (dashed dotted lines) for measurements with noise level $\sigma_N = 0.6$ and dip and dip direction obtained from an elliptical fracture forward model. Right figure: Comparison of synthetic front (solid lines) with ILSA-EKF front (dotted lines) and with noise level $\sigma_N = 0.6$ when correct dip and dip direction are used. The results are plotted every 20 timesteps.

Noise Level	Dip	Dip Direction
0.00	33.34	20.3
0.02	33.43	20.9
0.04	33.45	20.4
0.06	33.34	19.7
0.08	33.34	20.8

Table 1—Dip and dip direction obtained with the elliptical-fracture model.

S^s and S^{E-1} are the regions occupied by the actual and estimated fractures, and $\mathcal{A}[\cdot]$ is the area of the region.

The ILSA-EKF algorithm requires that the fracture orientation be known a priori, which is seldom the case in the field. To satisfy this condition, the simulation is carried out in a two-step fashion, where the fracture dip and dip direction are first obtained with an elliptical fracture forward model (Lecampion and Gunning 2007; Pandurangan et al. 2015). The ILSA-EKF model is then used to obtain the fracture footprint by fixing the dip and dip direction to the values obtained in the first step. In the TAL, the fracture dip, dip direction, width, and geometry are chosen as the state variables, and a simple persistence model is used to predict their values forward in time. The observation model on the basis of the analytical Okada solution is used. The dip and dip direction predicted by the TAL for different noise levels are summarized in **Table 1**.

For the surface array coordinates defined in Eq. 19, the synthetic measurements fall in the far-field regime with the resolution index in the range 2.7–14.5. Considering the far-field nature of the data, the EKF parameter Φ was chosen from the range (0.5–2), and convergence was achieved for $\Phi = 0.8$. **Fig. 3** shows the snapshots of the synthetic-fracture footprints (solid lines) corresponding to an initially radial fracture propagating in a linearly varying stress field, and those predicted by the ILSA-EKF algorithm (dotted lines), the TAL with an elliptical DD model (dashed dotted), using the synthetic tilt measurements with a noise level $\sigma_N = 6\%$, and assuming that the confining stress is absent. The results on the left correspond to the two-step inversion, where the fracture orientation was first obtained from the TAL. The predicted fronts show significant distortions that do not follow the synthetic front, and develop spurious bulges at latter times. This behavior can be mainly attributed to the errors introduced while estimating the dip angle with the TAL. This can be verified from the figure on the right that shows the same comparison when the TAL step is skipped, and the simulation is repeated with the correct dip and dip direction ($30^\circ, 20^\circ$). Here, the results show good agreement with the synthetic result in spite of the 6% Gaussian noise added to the data. This highlights the fact that even small

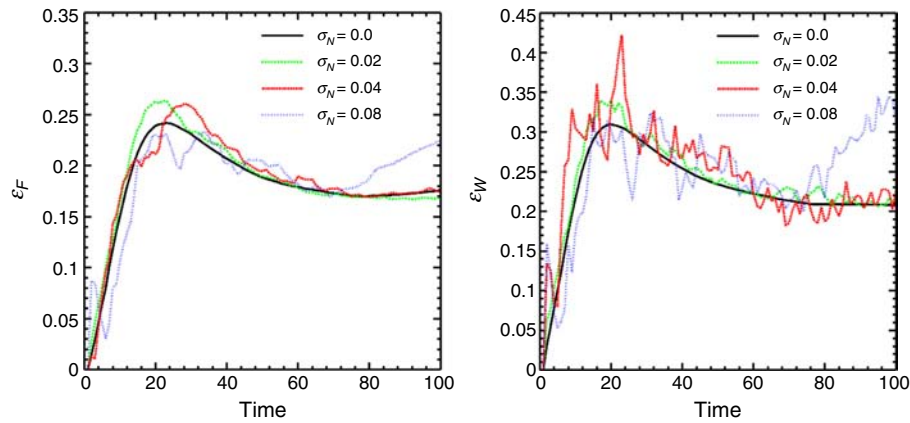


Fig. 4—Left figure: Relative footprint error (relative difference between the actual and estimated fracture geometry) at different noise levels. Right figure: Relative width error (relative difference between the actual and estimated fracture width) at different noise levels by use of synthetic data sets. The fracture dip and dip direction for the different noise levels are obtained from the TAL, and are summarized in Table 1.

errors in estimating the dip angles (close to 10% in this case) can significantly affect ILSA-EKF front predictions. However, despite the significant error in the dip angles, the ILSA-EKF scheme is able to capture the significant asymmetry in the hydraulic fractures that developed in the linearly varying stress field, which was used to generate the synthetic tilt data. Although the TAL analysis is also able to reasonably capture the fracture asymmetry, the predicted fracture footprints are smaller than those predicted by the ILSA-EKF scheme. The maximum fracture volume predicted by TAL and ILSA-EKF is 0.95 and 0.91 m³, respectively, which agrees well with the actual fracture volume of 0.94 m³ used for generating the synthetic data. In the TAL analysis, the fracture opening is constrained to obtain a physically reasonable solution. In contrast, the ILSA-EKF model solves the coupled system of Eq. 13 to compute the fracture opening as a function of time, which results in more-realistic estimates of the fracture opening and therefore the fracture footprint. The improved prediction of the fracture geometry by ILSA-EKF can provide improved resolution of the fracture geometry in field applications, including better estimates of fracture-height growth. This additional information provides critical feedback to optimize hydraulic-fracture treatments. The width and footprint errors for different noise levels are summarized in Fig. 4. Both error curves exhibit similar characteristics, peaking at a relatively early time and gradually reducing thereafter. Because the fracture front evolves with time, there is a reduction in the resolution index, and there is thus a gradual transition toward the near-field regime. Also, the EKF learns by assimilating more data with time, resulting in a smaller error covariance and more accurate estimates.

Field Study. The field data presented in this study were obtained from preconditioning trials carried out by the CSIRO at the Narrabri longwall coal mine, New South Wales, Australia. Longwall mining is an underground-mining technique for extracting relatively flat coal seams. During the mining operation, hydraulic roof supports are used to protect workers and equipment to allow the mining of the coal. As the mining progresses, the roof supports are moved forward along the longwall face, and the roof rock is allowed to cave into the void region behind the supports. If the roof is strong, failure does not occur immediately, and a large open void may form behind the supports. Failure of the rock above this void may then occur suddenly, significantly increasing the loads on the roof supports and potentially producing a dangerous wind blast because the air and gas in the void are displaced into the mine workings. Preconditioning with hydraulic fracturing is a rock-caving control technique in which hydraulic fractures are generated to weaken the roof rock and to promote earlier and more-uniform caving, thereby improving the safety conditions at the site (Jeffrey et al. 2013).

During the preconditioning treatment at Narrabri, multiple parallel fractures with a spacing of 2.5 m were generated from vertical boreholes at a depth of 140–175 m. Pressure monitoring and temperature logging in offset boreholes, positioned 10–30 m from the injection hole, were used to estimate fracture-arrival times and to ascertain if the fractures remained horizontal over a 30-m distance. In addition, a tiltmeter array consisting of 12 tiltmeters, secured firmly in 10-m deep holes around the injection well, was used to determine the fracture orientation and geometry. When a series of hydraulic fractures is started one after the other from different points along a borehole, they can alter the local stress field around them, thereby increasing the chances for a newly started fracture to develop asymmetrically. Therefore, the objective of this exercise was to determine whether the ILSA-EKF algorithm is able to provide some insight into the fracture asymmetry by comparing the predicted fracture front estimates with the intersection data recorded in the offset monitoring wells.

First, we present the results for Fracture 1 started from Borehole J (F1J) at a depth of 146.8 m. In this case, data from 11 tiltmeters were available. The fracturing treatments typically lasted approximately 45 minutes, but the tiltmeter data were collected over a larger time window, which included some time period before the start of injection and sometime after shut-in. Fig. 5 shows the raw data obtained from one of the tiltmeters used in the study. The raw data are first filtered to remove noise from external events such as instrument drift, vehicle movements and others. Random spikes in the data are then removed and substituted with a local signal after which the low-frequency noise is removed by fitting a trend function to the tilt data recorded before the actual fracturing treatment. Finally, this trend is subtracted from the denoised signal to extract the tilt signal induced by the hydraulic fracture, which is then used for further analysis with the ILSA-EKF algorithm.

The Young's modulus and Poisson's ratio of the conglomerate roof rock were measured from core samples (Jeffrey et al. 2013) and were found to be 20 GPa and 0.2, respectively. The dip and dip direction were first estimated with the TAL and were found to be 20° and 174°, respectively. The apparent dip angles were also estimated by knowing the depth of the intersections of the fractures with the offset boreholes. In this case, the fracture was found to be nearly horizontal with apparent dip angles between 0° and 5°. The apparent dip estimate, which was the result of a direct observation/measurement, was assumed to be correct with confidence, and therefore a smaller dip angle of 3° was used in the asymmetry analysis.

Fig. 6 shows the ILSA-EKF fracture footprints at different times in the fracture coordinate system with the origin (0, 0) at the injection point in Borehole J. The black-dashed contour lines refer to the fracture footprints before shut-in, and the green-solid

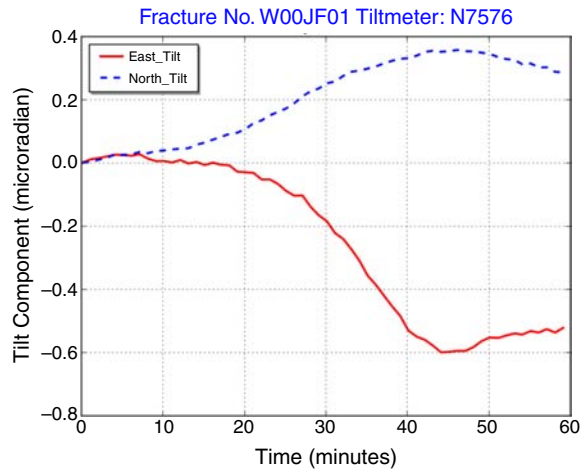
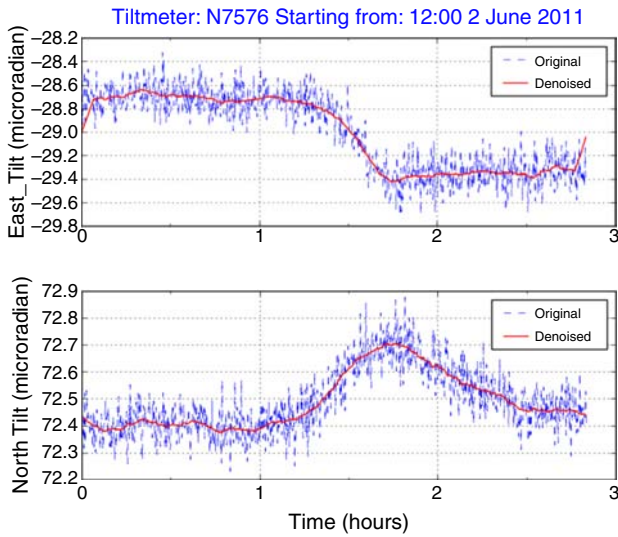


Fig. 5—Left figure: The original measured noisy data and the denoised signal from one tiltmeter corresponding to Fracture 1 in Borehole J. Right figure: Tilt signal induced by the hydraulic fracture after subtracting the trend that is used in the ILSA-EKF analysis.

lines show the footprints after shut-in. The circles represent the boreholes. Fig. 7 shows a 3D view of the fracture footprints with the z-axis representing the time in minutes. The vertical lines correspond to the injection Borehole J and offset Boreholes A, C, and E, with blobs indicating the measured intersection times (red) and estimated intersection times (green), in minutes. It can be seen from the contour plot that the fracture growth is asymmetric about the injection Borehole J, with the growth preferentially

being in the negative ζ direction. F1J was the first fracture in the borehole, and therefore, a somewhat symmetric profile was expected. Hence, the exact reason for the asymmetry is not known. The footprints after shut-in also show spurious herniation. Recall that such spurious bulges were also observed in the earlier investigation with the synthetic data when the incorrect fracture orientation was used. However, with field data, it is difficult to verify if the herniations are the result of incorrect fracture orientation or noise in the data.

The measured intersection times with offset boreholes serve as a reference to compare and validate the ILSA-EKF footprints. Table 2 shows the measured intersection times for F1J with Boreholes A, C, and E. Fig. 6 also shows the shortest distance in meters between each borehole and the point on the fracture front closest to the borehole at the measured intersection times, which is indicated by a triangle. The number (7.2) for example refers to the shortest distance (m) from the triangle closest to the Borehole E at time $t = 9$ minutes. We have used this as an error measure to

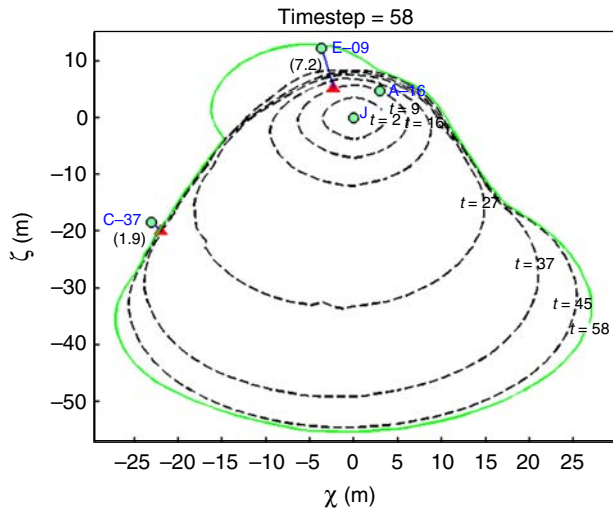


Fig. 6—Left figure: Plot of the ILSA-EKF fracture footprints at different times for Fracture 01 in orthogonal view with the origin (0, 0) at the injection point in Borehole J and the offset monitor boreholes (A, C, E). The fracture dip and dip direction are not represented in this orthogonal view. The black-dashed contours indicate footprints before shut-in, and the solid-green line shows the results after shut-in. The red triangles show the location of the closest points on the $t = 9$ and $t = 37$ ILSA-EKF footprints corresponding to the observed arrival times at Boreholes E and C, respectively. The number (7.2) refers to the shortest distance (m) from the triangle closest to Borehole E at time $t = 9$, and the number (1.9) refers to the shortest distance (m) from the triangle closest to Borehole C at time $t = 37$. The shortest distance between Borehole E and the closest ILSA-EKF footprint at any time during the inversion was 0 m (at time $t = 58$) and the shortest distance between Borehole C and the closest ILSA-EKF footprint at any time during the inversion was 1.6 m (at time $t = 58$). Note that the borehole locations have been rotated to the fracture coordinate system.

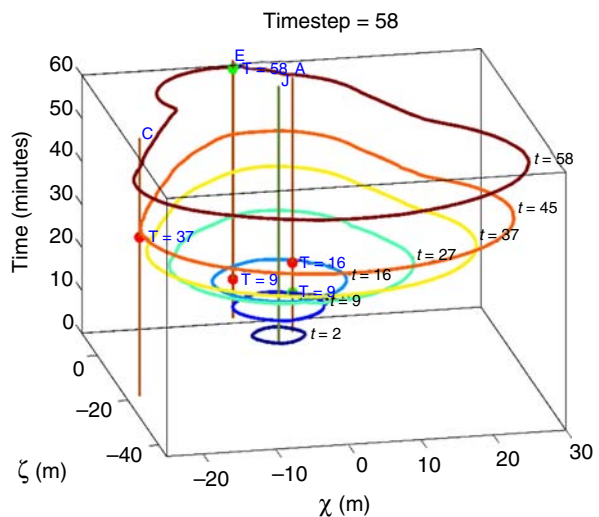


Fig. 7—Right figure: Shows the 3D view of fracture footprints with the z-axis representing time. The vertical lines correspond to the Injection Borehole J and the offset boreholes A, C, and E. The figure also shows the measured intersection times (red) observed in the field, and intersection times obtained from the simulation (green), in minutes. Note that the borehole locations have been rotated to the fracture coordinate system.

Date	Fracture Number	Borehole	Depth (m)	Start of Injection (t_1)	Intersected Borehole	Intersection Time (t_2)	$\Delta t = t_2 - t_1$
2/6/2011	1	J	146.8	13:01:10	E	13:09:56	0:08:46
					C	13:38:12	0:37:02
					A	13:17:00	0:15:50
22/9/2011	3	AA	168.1	14:33	AB	15:05	0:32
					AC	14:40	0:07
23/9/2011	5		175.6	09:26	AC	09:52	0:26

Table 2—Measured intersection times for different fractures with monitoring holes.

compare the simulation results. The offset borehole monitoring shows that **F1J** intersects Borehole **A** at 16 minutes, whereas in the simulation, it takes 9 minutes for the fracture to intersect Borehole **A**. The arrival time at Borehole **A** was determined by pressure monitoring in which the intersection time was taken as the time when the pressure exceeded the vertical or minimum principal stress. The arrival time is thus deduced from the pressure plots, and can sometimes be complicated, unlike temperature monitoring (used in Boreholes **E** and **C**) in which arrival times are sharper and more clear-cut. This might have resulted in some of the discrepancy with the simulated intersection times. The predicted fracture front does not show intersection with Borehole **C** although it reaches very close (1.9 m) to it at the observed intersection time of 37 minutes. The borehole-survey process does contain an uncertainty in the determined bottomhole location, which is typically approximately 1 m at depths of 200 m. Therefore, an error of 1.9 m in ILSA-EKF arrivals compared with the plotted borehole location can be regarded as insignificant. The simulation also shows interaction with Borehole **E** only at 58 minutes against the observed time of 9 minutes. Because the simulation shows that intersection occurs only after shut-in, it is most likely a degenerate case and cannot be considered as a true measure of the arrival time. Therefore, we have used the distance error to indicate the distance from the borehole to the fracture front at the measured intersection time $t = 9$. It can be seen that the distance error (7.2 m) in this case is larger compared with that of **C** (1.9 m). As per the intersection data, **F1J** grows into Borehole **E** earlier during the treatment (9 minutes), but grows into Borehole **C** much later, toward the end of the fracture treatment (37 minutes). Previously, with synthetic data, we had seen that the ILSA-EKF predictions improve with time as the filter assimilates more data. At $t = 37$ minutes, the filter has already assimilated considerable data compared with time $t = 9$. Also, the fracture

dimensions and volume are much larger at $t = 37$, resulting in a stronger tilt signal and therefore a larger signal–noise ratio. These are the probable reasons for the relatively larger distance error observed for Borehole **E** compared with Borehole **C**. A comparison between the measured tilt vectors and the estimated tilt vectors at the end of injection is shown in **Fig. 8**. It can be observed that the ILSA-EKF algorithm is able to reasonably fit the observed tilt data, in spite of the far-field nature of the data. The radially divergent tilt pattern is characteristic of subhorizontal fractures. **Fig. 9** shows the predicted final fracture footprint at $t = 58$ minutes superimposed on the site layout, which shows the borehole locations and tiltmeter positions.

In the synthetic example presented in the previous section, we had compared the mismatch between the actual and the estimated fracture geometry at different noise levels. In the field example presented here, the actual fracture geometry is unknown whereas intersection data provided a means to indirectly validate the ILSA-EKF estimates. Therefore, to study the influence of tiltmeter data on model prediction, the tilt data were corrupted by a noise amplitude σ where σ refers to the standard deviation of the measured signal in each of the tiltmeters, and the ILSA-EKF simulation was repeated with the noisy signal. The addition of noise to the tilt signal can also affect the predicted dip angle. Hence, the simulation was carried out in a two-step fashion, in which the fracture dip and dip-direction were first obtained with the elliptical DD model in the TAL to determine the change in dip angle as a result of introducing the noise, and then the ILSA-EKF simulation was carried out with a fixed dip and dip direction. The effect of the noise level on the dip angle is predicted with the TAL; then, the predicted change in the dip angle from the TAL is added to the dip angle used in the ILSA-EKF simulation ($3^\circ + \text{changes}$), to reflect the influence of noise of tilt measurements. For example,

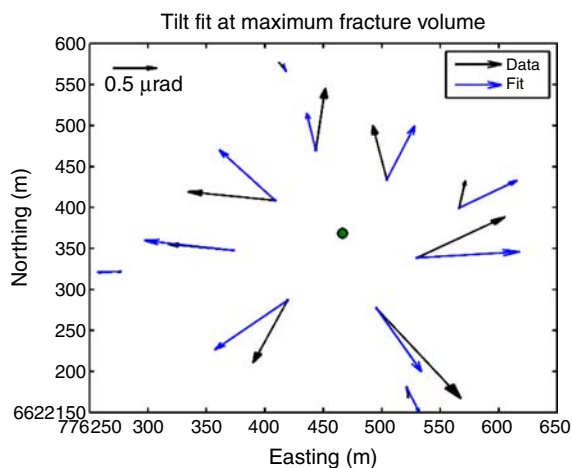


Fig. 8—Left figure: Tilt vectors at the end of injection for Fracture 01 in Borehole J. The divergent radial pattern is typical of horizontal fractures.

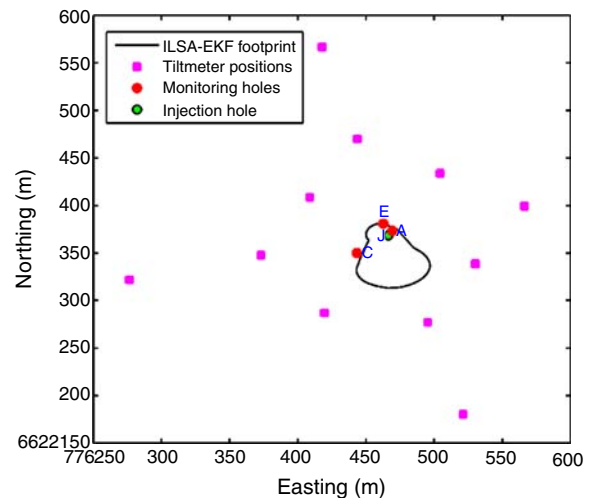


Fig. 9—Right figure: Site layout showing the fracture footprint predicted by ILSA-EKF at the end of injection, the injection and monitoring boreholes, and the locations of the tiltmeters.

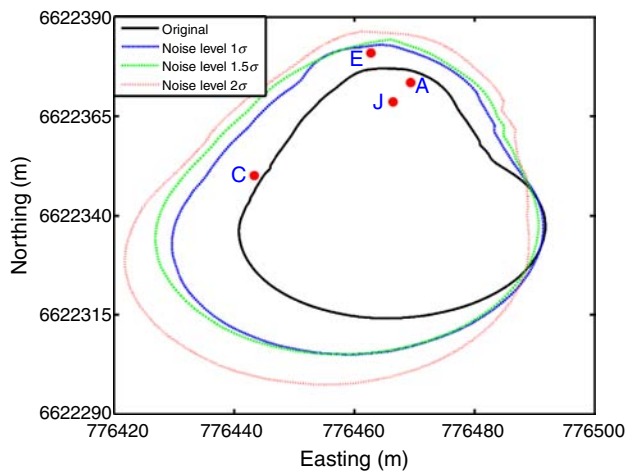


Fig. 10—Comparison of ILSA-EKF fracture footprints at the end of injection at different noise levels with the original fracture footprint for Fracture 1 in Borehole J and the offset monitor boreholes (A, C, E).

if the TAL predicts a change of 9° in the dip angle for a given noise level, the dip angle used in the ILSA-EKF is $3^\circ + 9^\circ$. The change in dip angles corresponding to noise levels 1, 1.5, and 2σ were 6° , 9° , and 12.7° . **Fig. 10** shows a comparison between the fracture footprints at the end of injection ($t = 45$ minutes) for different noise levels with the original footprint obtained before the addition of noise. Although the shape of the estimated fractures at different noise levels is similar to the original estimates, the fracture area/size is different and shows an increase with increased noise levels. Because the dip angle is strongly coupled to the fracture geometry, both the increase in tilt magnitude with the addition of noise and corresponding change in dip angle are responsible for the increase in the fracture footprint. The root-mean-square (RMS) error between measured and estimated tilt vectors at the end of injection was used to compare the quality of

the resulting fit at different noise levels. The RMS error at the end of injection for noise levels 1, 1.5, and 2σ were 0.59, 0.69, and $0.83 \mu\text{rad}$, respectively. In comparison, the RMS error for the original signal was $0.48 \mu\text{rad}$, which clearly shows that the quality of the resulting fit deteriorates with an increase in noise level although the fracture volume in all the cases is less than the injected fluid volume.

Next, we present the results for Fractures 03 and 05 started at a second different test site from Borehole AA at a depth of 168.1 and 175.6 m, respectively. In this case, data from 12 tiltmeters were available. In the first analysis step, the TAL was used to obtain an estimate of the fracture dip and dip-direction, which were 21° , 310° , and 13° , 330° for Fractures 03 and 05, respectively. As before, the data from the offset boreholes were also used to obtain an estimate of the apparent dip angle. On the basis of these results, the dip angle was fixed at 5° , and the dip directions were fixed at 310° and 330° for Fractures 03 and 05, respectively. **Figs. 11 and 12** show the plan and 3D views of the ILSA-EKF fracture footprints at different times, in the fracture coordinate system with the origin (0, 0) at the injection point in Borehole AA. The black-dashed and green-contour lines refer to the fracture footprints before and after shut-in respectively. In **Fig. 11**, it can be observed that Fracture 03 develops asymmetrically with respect to Borehole AA. Previously placed fractures cause stress changes and perhaps an even bigger pore-pressure change and concomitant stress changes. In this case, Fracture 02 was placed 45 minutes before Fracture 03 in Borehole AA, at a depth of 178.1 m. This might have locally altered the stress field around Fracture 03 and caused the observed asymmetry.

As before, intersection times with offset Boreholes AB and AC, summarized in Table 2, were used as a reference to validate the ILSA-EKF footprints. In **Fig. 11**, it can be observed that the fracture front grows into Borehole AC (7 minutes), much earlier than AB (32 minutes). The simulation shows intersection with both holes, but the ILSA-EKF intersection time of 45 minutes with AC occurs after shut-in. Pressure monitoring was used in AC, and temperature monitoring was used in AB, which means that the observed arrival time of 7 minutes at Borehole AC might be subject to a larger error than that in AB. This, along with the

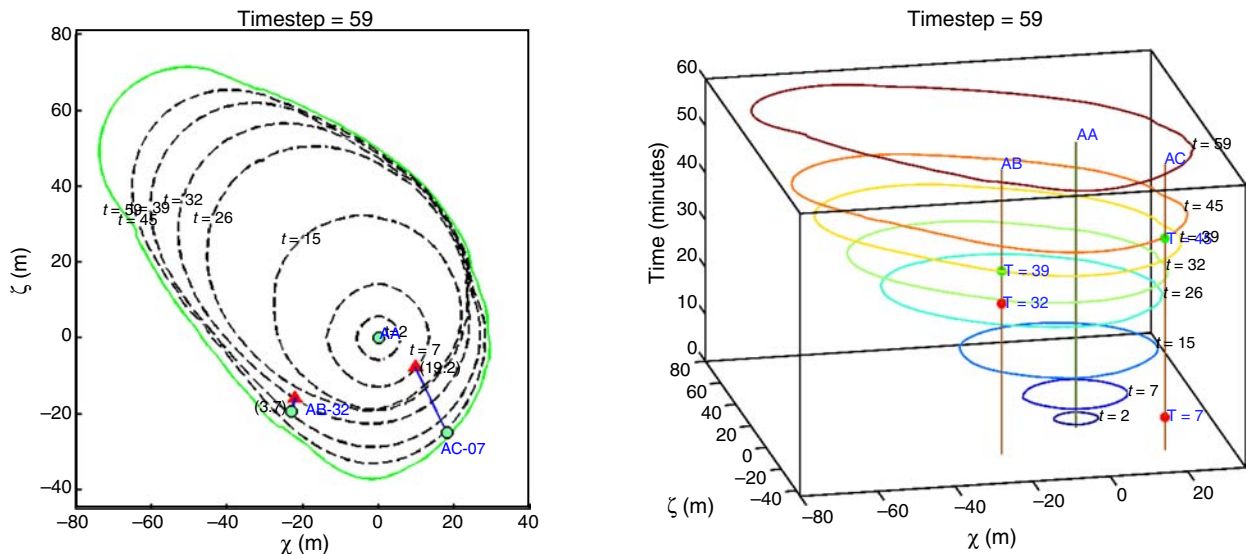


Fig. 11—Left figure: Plot of the ILSA-EKF fracture footprints at different times for Fracture 03 in orthogonal view with the origin (0, 0) at the injection point in Borehole AA and the offset monitor boreholes (AB, AC). The fracture dip and dip direction are not represented in this orthogonal view. The black-dashed contours indicate footprints before shut-in, and the solid-green line shows the results after shut-in. The red triangles show the location of the closest points on the $t = 7$ and $t = 32$ ILSA-EKF footprints corresponding to the observed arrival times at Boreholes AC and AB, respectively. The number (19.2) refers to the shortest distance (m) from the triangle closest to Borehole AC at time $t = 7$, and the number (3.7) refers to the shortest distance (m) from the triangle closest to Borehole C at time $t = 32$. Right figure: Shows 3D view of fracture footprints with the z-axis representing time. The vertical lines correspond to the Injection AA and the offset Boreholes AB and AC. The figure also shows the measured intersection times (red) observed in the field, and intersection times obtained from the simulation (green), in minutes. Note that the borehole locations have been rotated to the fracture coordinate system.

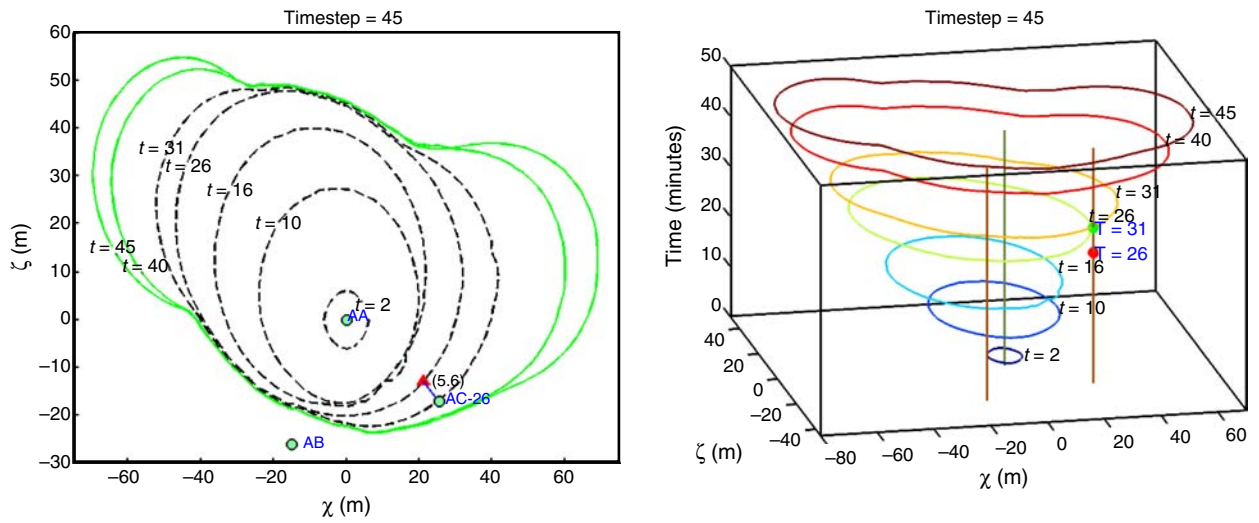


Fig. 12—Left figure: Plot of the ILSA-EKF fracture footprints at different times for Fracture 05 in orthogonal view with the origin (0, 0) at the injection point in Borehole AA and the offset monitor boreholes (AB, AC). The fracture dip and dip direction are not represented in this orthogonal view. The black-dashed contours indicate footprints before shut-in, and the solid-green line shows the results after shut-in. The red triangles show the location of the closest points on the $t = 26$ ILSA-EKF footprint corresponding to the observed arrival time at Boreholes AC. The number (5.6) refers to the shortest distance (m) from the triangle closest to Borehole AC at time $t = 26$. Right figure: Shows 3D view of fracture footprints with the z-axis representing time. The vertical lines correspond to the Injection AA and the offset Boreholes AB and AC. The figure also shows the measured intersection times (red) observed in the field, and intersection times obtained from the simulation (green), in minutes. Note that the borehole locations have been rotated to the fracture coordinate system.

fact that the observed intersection time occurs close to the start of injection, explains why the distance error is larger (19.2m) for Borehole AC. In the case of Borehole AB, intersection occurs later in the simulation, allowing the filter to assimilate more data, which is why the ILSA-EKF time estimate (39 minutes) shows better agreement with the measured intersection time (32 minutes), with a smaller distance error of 3.2 m.

In the case of Fracture 05, the simulation shows intersection with AC at 31 minutes against the observed time of 26 minutes, with a distance error of 5.2 m. Considering that pressure monitoring was used in this hole, this estimate is very reasonable. It is interesting to observe that the simulation shows no intersection with Borehole AB, exactly as was observed at the site. This demonstrates that the ILSA-EKF is able to make a reasonable prediction of the fracture front and is also able to capture fracture asymmetry. **Fig. 13** shows the predicted final fracture footprint superimposed on the site layout, which shows the borehole locations and tiltmeter positions. **Fig. 14** shows the measured and the

estimated tilt vectors at the end of injection, which once again shows a radially diverging pattern typically associated with sub-horizontal fractures.

Fig. 15 shows the average fracture width and the width at the wellbore for all the three fractures discussed so far. The wellbore width is the width at the injection point, and the average width is the simple average over all elements in the Eulerian mesh. If we assume the fracture to be a line crack opened by a net pressure that is linearly varying within the fracture, the opening profile would be ellipsoidal with maximum width at the center (Valkó and Michael 1995). Hence, we find that the wellbore width is higher than the average width for Fractures 03 and 05, and initially for Fracture 01. The fracture center coincides with the injection point for a symmetric fracture, but moves farther away from the injection point as the fracture develops asymmetry. In the case of Fracture 01, the fracture, which is initially symmetric, develops strong asymmetry at later times. This implies that the fracture center has moved significantly away from the injection point,

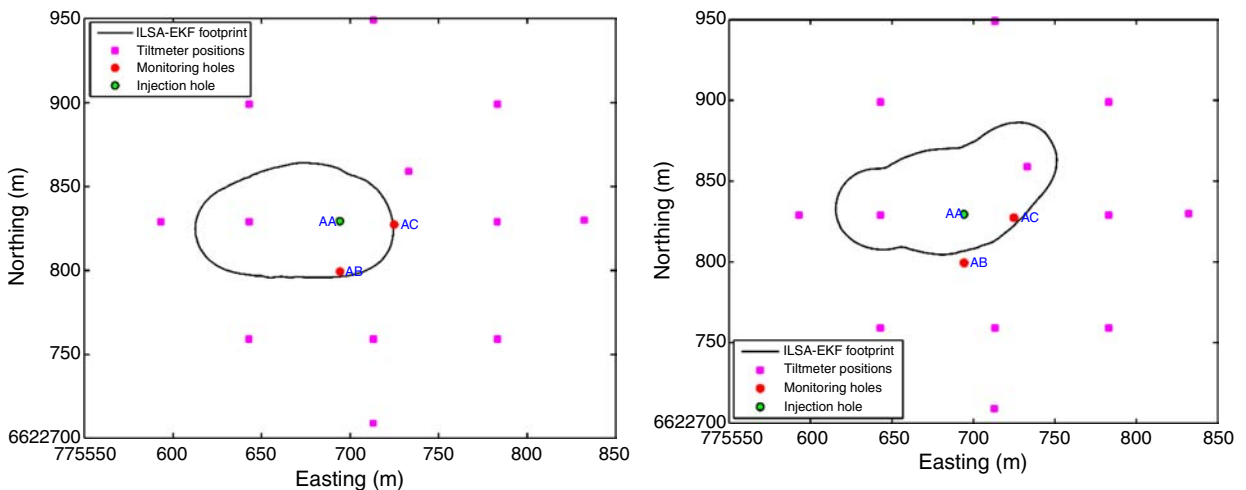


Fig. 13—Site layout showing the fracture footprint predicted by ILSA-EKF at the end of injection for Fracture 03 (left) and Fracture 05 (right), the injection and monitoring boreholes, and the locations of the tiltmeters. Note that borehole locations shown are surface locations in this figure.

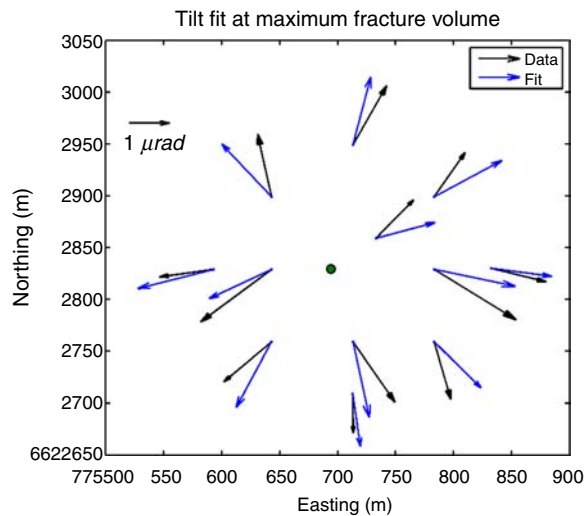
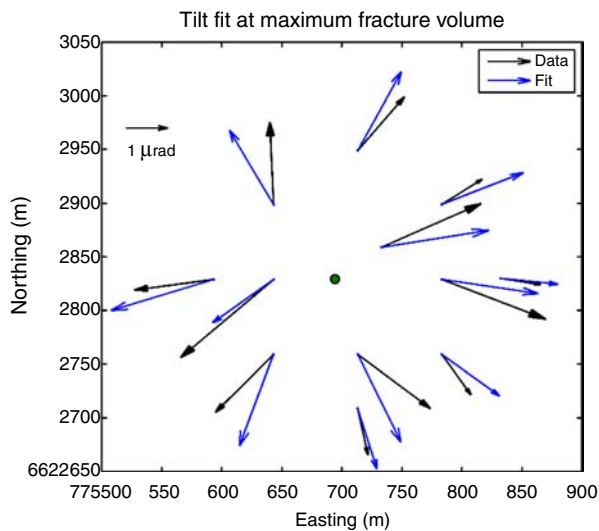


Fig. 14—Tilt vectors at the end of injection for Fracture 03 (left) and Fracture 05 (right).

which is now toward one end of the fracture. Therefore, in the case of Fracture 01, the wellbore width is smaller than the average width at later times and also shows large fluctuations.

Fig. 16 shows a comparison between the estimated fracture volume and injected-fluid volume for all three fractures. The injected-fluid volume is the cumulative volume of fluid injected into the well during the fracture treatment. The predicted fracture-volume profile is consistent with the injected-fluid volume in all three cases. The volume increases until the end of injection, and there is a drop in volume as the fracture faces close because of fluid loss and decreasing net pressure. Fracture 03 shows an increase in volume above the injected volume after shut-in, which is physically not possible. The reason for this behavior is not clear. A possible reason is that the residual tilt signals from Fracture 02 placed 45 minutes before Fracture 03 in Borehole AA could have affected the tilt signals from Fracture 03.

In all the three cases, the fracture volume is less than the injected volume, meaning that some amount of fluid leaks off into the formation or there is some spurious leakoff. There are several possible mechanisms other than the leakoff that would affect the fracture volume and reduce the tilt signal. The fractures are contained in a conglomerate, which most probably has a Young's modulus similar to that of the overburden rock. However, the coal seam, which is 6 to 7 m thick and is located 5 to 10 m below the

fracture plane, has a Young's modulus that is an order of magnitude lower than that of the rock. The drainage of water and gas to variable degrees from the coal seam before the fracturing will cause some shrinkage of the softer coal seam. Consequently, some of the deformation caused by the actual fracture may be absorbed by the softer coal layer, resulting in smaller tilt signals at the surface. The conglomerate has low permeability but does contain natural fractures, so leakoff can occur. Shearing on faults and fractures is another energy-dissipation mechanism that has not been accounted for in the current study. The other loss process is fracture intersection with adjacent boreholes and fluid loss from these boreholes. Any or all these factors could have contributed to a reduced fracture volume.

Conclusion

In this work, we proposed a technique that uses tilt data to detect asymmetric hydraulic-fracture growth in a homogeneous elastic half-space. The algorithm uses the EKF to integrate the dynamic ILSA scheme with tilt data to obtain real-time estimates of the fracture footprint. The highlight of the ILSA-EKF scheme is that only the fracture width is treated as the state variable in the EKF,

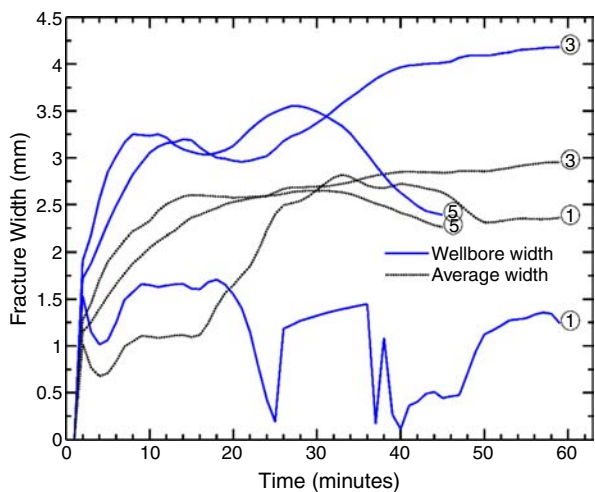


Fig. 15—Plot of the average fracture width and the width at the wellbore for Fracture 01 in Borehole J, and Fractures 03 and 05 in Borehole AA.

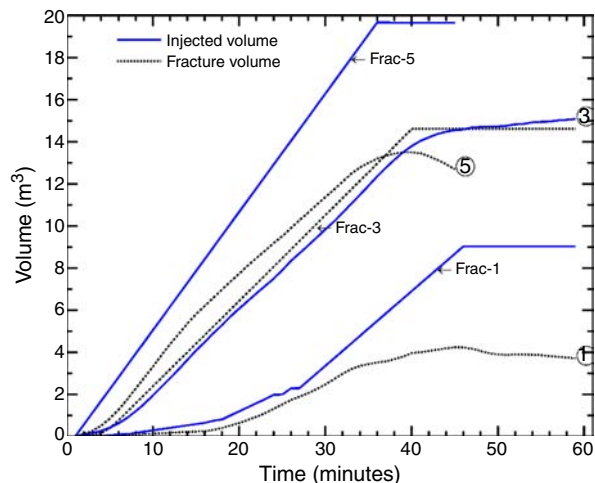


Fig. 16—Comparison of the injected-fluid volume (solid lines) and the estimated fracture volumes (dashed lines) for Fractures 01, 03, and 05. The fracture volume predicted by ILSA-EKF and injected-fluid volumes (in parentheses) at the end of injection for Fractures 01, 03, and 05 were, respectively, 4.2 (9.3) m³, 13.8 (16) m³, and 13.1 (19.6) m³, respectively.

and the fracture boundary is located with the ILSA algorithm using the tip asymptotic relationship, avoiding the need to parametrize the fracture boundary. Further, the scheme uses the Okada half-space solution as a building block to establish the observation model (forward model) to relate the fracture geometry to the observed tilt. This is a more faithful representation of a fracture propagating below the surface in which the characteristic length of the fracture is not too small compared with the fracture depth, and the tilt measurements are near the ground surface. The fracture dip and dip direction, together with the fracture geometry, are required to completely describe the fracture. Because the Okada model provides analytical expressions for the displacements and tilts caused by a given fracture, it is computationally highly efficient.

Numerical experiments involving synthetic data show that the algorithm is able to filter out measurement noise, but an error in dip angle can have a significant impact on the predicted footprint and may result in spurious herniations. After validating the ILSA-EKF algorithm with the synthetic data set and ensuring that the algorithm provides a reasonable estimate of the fracture geometry (Fig. 3), we have used it to further analyze field data. The analysis of field tilt data collected during preconditioning trials and corresponding to three different hydraulic fractures showed that the ILSA-EKF scheme was able to make reasonable estimates of the fracture footprint, which agreed well with the intersection data from offset monitoring boreholes. In the case of field data, the exact geometry of the developing fracture is unknown. The measured intersection times with offset boreholes were therefore used as a “reference” to validate the ILSA-EKF footprints. The “distance error” is defined as the distance between an intersection borehole and the closest point on the ILSA-EKF fracture front at the time the fracture intersects the borehole. The distance error is thus used to provide a quantitative way to indicate the extent to which the ILSA-EKF predictions differ from the expected geometry on the basis of the intersection data. Considering the uncertainties associated with determining the intersection times, the distance errors were relatively small, meaning that ILSA-EKF predictions most likely reflect reality and correlate fairly well with the intersection field data. Further, for Fracture 05, the ILSA-EKF front registered no intersection with the offset Borehole **AB**, in agreement with the field observation, showing that the ILSA-EKF algorithm is able to capture fracture asymmetry. The filter performance also showed improvement with time, which was evident from the smaller distance errors for intersections that occurred toward the end of injection.

Typically, the conglomerate in which hydraulic fracturing is performed consists of multiple layers, each with different material properties such as Young’s modulus, toughness, and Poisson’s ratio and others. Furthermore, the stress distribution is rarely homogeneous, and the rock permeability means that a portion of the injected fluid will leak into the surrounding formation. There are also other factors such as stress shadows from previous fractures, soft coal seams, fluid loss to natural fractures, and others that have not been explicitly accounted for in the dynamic ILSA model. These features were omitted to make the problem computationally feasible without ignoring the essential physics of the problem. However, these unmodeled factors, which we have termed as “unmodeled dynamics,” do have an impact on the measured tilt signal. The ILSA-EKF algorithm presented in this paper does therefore, to a certain extent, account for these missing features in the models. When the feedback from the tilt measurements is assimilated with the dynamic model through the EKF to obtain the maximum likelihood estimates of the fracture widths and geometry, we are, in some sense, indirectly accounting for these factors and therefore expect that the predicted geometry that we obtain is a more realistic representation of what is happening in reality. For example, the ILSA-EKF predicts a volume smaller than the injected volume, possibly caused by unmodeled leakoff.

The ILSA-EKF algorithm is a novel approach for integrating mathematical modeling and monitoring techniques for a better evaluation of hydraulic-fracture treatments. Although the algorithm, in its current form, can be used for real-time mapping of

hydraulic fractures, there is scope to improve its efficiency and accuracy by making further improvements to the forward model to reduce the “unmodeled dynamics.” As seen in the synthetic example, the fracture dip and orientation can have a significant impact on the predicted results, and, therefore, the immediate goal would be to obtain more-accurate estimates of these quantities. Though the ILSA-EKF algorithm uses the half-space observation model, the ILSA scheme still considers the fracture to be in an infinite homogeneous medium, defined by a single value of Young’s modulus and Poisson’s ratio. Therefore, a possible improvement to the ILSA algorithm includes the use of half-space kernels to determine the elastic fracture opening (Zhang et al. 2002), and accounting for the heterogeneous nature of the rock mass with a multilayer elastic model, in which the elastic properties vary across each layer (Peirce and Siebrits 2001; Siebrits and Peirce 2002). Leakoff is an important aspect of hydraulic fracturing, and obtaining a better quantification of it would be very useful. If the conglomerate is highly porous, leakoff can result in a poroelasticity-induced tilt signal, which has to be separated from the measured tilt signal to obtain more-realistic estimates of the fracture geometry. The focus of our future work will be to develop a unified algorithm that addresses some of these issues, and to test it across a wide range of field conditions.

Nomenclature

$\mathcal{A}(\cdot)$	= area function
D	= displacement discontinuity
E	= Young’s modulus, GPa
E'	= plane-strain modulus, $E' = E/(1 - \nu^2)$, GPa
$f(\cdot)$	= dynamic fracture-propagation model
F	= Jacobian of the function $f(\cdot)$
\mathcal{H}	= scaled Green’s-function operator
$H(\cdot)$	= observation model
K	= Kalman gain matrix
n	= unit normal vector
p	= net fluid pressure, Pa
p_f	= fluid pressure, Pa
q	= normally distributed process noise, $q \approx N(0, \Gamma_q)$
Q	= fluid-injection rate, m^3/s
s	= source term at wellbore
S	= region occupied by fracture
t	= time, seconds
T	= signed distance function
u	= displacement, m
U	= displacement fundamental solution
v	= normally distributed measurement noise, $v \approx N(0, \Gamma_v)$
w	= fracture opening, m
\hat{w}	= predicted fracture opening, m
x	= model state vector
y	= observation vector
Z	= signed-distance surface
$\delta(\cdot)$	= Dirac Delta function, $1/m$
θ	= fracture dip, degrees
$(180 - \phi)$	= dip direction, degrees
ξ	= distance to fracture perimeter, m
μ	= fluid dynamic viscosity, Pa·s
μ'	= fluid dynamic viscosity, $\mu' = 12\mu$, Pa·s
ν	= fluid tip velocity, m/s
β_{mo}	= dimensionless constant, $\beta_{mo} = 2^{1/3}3^{5/6}$
\mathcal{E}_w	= width error
\mathcal{E}_F	= footprint error
Φ	= EKF parameter
χ	= x -coordinate of rectangular mesh
ζ	= y -coordinate of rectangular mesh
ζ	= depth of tiltmeter array, m
ω	= rotational movement, radians
Δt	= timestep
σ_0	= minimum principal stress, MPa
σ_N	= noise amplitude
Γ_q	= process-noise covariance matrix
Γ_v	= measurement-noise covariance matrix

ε, γ = scaling parameters
 ∂S = fracture-front position

Acknowledgment

Permission to publish from CSIRO is gratefully acknowledged. Anthony Peirce gratefully acknowledges the grant support of NSERC.

References

- Adachi, J., Siebrits, E., Peirce, A. et al. 2007. Computer Simulation of Hydraulic Fractures. *International Journal of Rock Mechanics and Mining Sciences* **44**: 739–757. <https://doi.org/10.1016/j.ijrmm.2006.11.006>.
- Bennett, C. O., Rosato, N. D., Reynolds, A. C. et al. 1983. Influence of Fracture Heterogeneity and Wing Length on the Response of Vertically Fractured Wells. *SPE J.* **23**: 219–230. SPE-9886-PA. <https://doi.org/10.2118/9886-PA>.
- Cipolla, C. L. and Wright, C. A. 2000. State-of-the-Art in Hydraulic Fracture Diagnostics. Presented at the SPE Asia Pacific Oil and Gas Conference and Exhibition, Brisbane, Australia. SPE-64434-MS. <https://doi.org/10.2118/64434-MS>.
- Davis, P. M. 1983. Surface Deformation Associated With a Dipping Hydrofracture. *J. Geophys. Res.* **88**: 5826–5834. <https://doi.org/10.1029/JB088iB07p05826>.
- Gelb, A. (ed.). 1974. *Applied Optimal Estimation*. MIT Press.
- Jeffrey, R. G. 1996. Asymmetrically Propped Hydraulic Fractures. *SPE Prod & Fac* **11**. SPE-28079-PA. <https://doi.org/10.2118/28079-PA>.
- Jeffrey, R. G., Chen, Z. R., Mills, K. W. et al. 2013. Monitoring and Measuring Hydraulic Fracturing Growth During Preconditioning of a Roof Rock Over a Coal Longwall Panel. In *Effective and Sustainable Hydraulic Fracturing*, ed. R. Jeffrey. InTech.
- Lecampion, B., Jeffrey, R., and Detournay, E. 2005a. Resolving the Geometry of Hydraulic Fractures From Tilt Measurements. *Pure Appl. Geophys.* **162**: 2433–2452. <https://doi.org/10.1007/s00024-005-2786-4>.
- Lecampion, B., Jeffrey, R., and Detournay, E. 2005b. Resolving the Geometry of Hydraulic Fractures From Tilt Measurements. *Pure Appl. Geophys.* **162**: 2433–2452. <https://doi.org/10.1007/s00024-005-2786-4>.
- Lecampion, B. and Gunning, J. 2007. Model Selection in Fracture Mapping From Elastostatic Data. *International Journal of Solids and Structures* **44**: 1391–1408. <https://doi.org/10.1016/j.ijsolstr.2006.06.022>.
- Montgomery, C. T. and Smith, M. B. 2010. Hydraulic Fracturing: History of an Enduring Technology. *J Pet Technol* **62** (12): 26–40. SPE-1210-0026-JPT. <https://doi.org/10.2118/1210-0026-JPT>.
- Okada, Y. 1992. Internal Deformation Due to Shear and Tensile Faults in a Half-Space. *Bull. of the Seismological Society of America* **82** (2): 1018–1040. [https://doi.org/10.1016/0148-9062\(86\)90674-1](https://doi.org/10.1016/0148-9062(86)90674-1).
- Olson, J. E., Du, Y., and Du, J. 1997. Tiltmeter Data Inversion With Continuous, Non-Uniform Opening Distributions: A New Method for Detecting Hydraulic Fracture Geometry. *International Journal of Rock Mechanics and Mining Sciences* **34** (3–4): 236.e1–236.e10. [https://doi.org/10.1016/S1365-1609\(97\)00120-2](https://doi.org/10.1016/S1365-1609(97)00120-2).
- Pandurangan, V., Chen, Z., and Jeffrey, R. G. 2015. Mapping Hydraulic Fractures From Tiltmeter Data Using the Ensemble Kalman Filter. *Int. J. Numer. Anal. Meth. Geomech.* **40** (4): 546–567. <https://doi.org/10.1002/nag.2415>.
- Peirce, A. P. and Siebrits, E. 2001. Uniform Asymptotic Approximations for Accurate Modeling of Cracks in Layered Elastic Media. *International Journal of Fracture* **110**: 205–239. <https://doi.org/10.1023/A:1010861821959>.
- Peirce, A. and Detournay, E. 2008. An Implicit Level Set Method for Modeling Hydraulically Driven Fractures. *Computer Methods in Applied Mechanics and Engineering* **197**: 2858–2885. <https://doi.org/10.1016/j.cma.2008.01.013>.
- Peirce, A. and Rochinha, F. 2012. An Integrated Extended Kalman Filter–Implicit Level Set Algorithm for Monitoring Planar Hydraulic Fractures. *Inverse Problems* **28**: 15009. <https://doi.org/10.1088/0266-5611/28/1/015009>.
- Peirce, A. 2015. Modeling Multi-Scale Processes in Hydraulic Fracture Propagation Using the Implicit Level Set Algorithm. *Computer Methods in Applied Mechanics and Engineering* **283**: 881–908. <https://doi.org/10.1016/j.cma.2014.08.024>.
- Rochinha, F. A. and Peirce, A. 2010. Monitoring Hydraulic Fractures: State Estimation Using an Extended Kalman Filter. *Inverse Problems* **26**: 25009. <https://doi.org/10.1088/0266-5611/26/2/025009>.
- Siebrits, E. and Peirce, A. P. 2002. An Efficient Multi-Layer Planar 3D Fracture Growth Algorithm Using a Fixed Mesh Approach. *Int. J. Numer. Meth. Engng.* **53**: 691–717. <https://doi.org/10.1002/nme.308>.
- Valkó, P. and Michael, J. E. 1995. *Hydraulic Fracture Mechanics*. New York: Wiley.
- Warpinski, N. R., Griffin, L. G., Davis, E. J. et al. 2006. Improving Hydraulic Fracture Diagnostics by Joint Inversion of Downhole Microseismic and Tiltmeter Data. Presented at the SPE Annual Technical Conference and Exhibition, San Antonio, Texas, USA, 24–27 September. SPE-102690-MS. <https://doi.org/10.2118/102690-MS>.
- Wright, C. A., Davis, E. J., Minner, W. A. et al. 1998. Surface Tiltmeter Fracture Mapping Reaches New Depths—10,000 Feet and Beyond? Presented at the SPE Rocky Mountain Regional/Low-Permeability Reservoirs Symposium, Denver, 5–8 April. SPE-39919-MS. <https://doi.org/10.2118/39919-MS>.
- Wu, R., Bunger, A. P., Jeffrey, R. G. et al. 2008. A Comparison of Numerical and Experimental Results of Hydraulic Fracture Growth Into a Zone of Lower Confining Stress. Presented at the the 42nd US Rock Mechanics Symposium (USRMS), San Francisco, 29 June–2 July. ARMA-08-267.
- Yang, X.-M. and Davis, P. M. 1986. Deformation Due to a Rectangular Tension Crack in an Elastic Half-Space. *Bull. of the Seismological Society of America* **76** (3): 865–881.
- Zhang, X., Detournay, E., and Jeffrey, R. 2002. Propagation of a Penny-Shaped Hydraulic Fracture Parallel to the Free-Surface of an Elastic Half-Space. *International Journal of Fracture* **115**: 125–158. <https://doi.org/10.1023/A:1016345906315>.

Venkataraman Pandurangan is a research scientist in the hydraulic-fracturing group at CSIRO. Previously, he worked for the Fraunhofer Institute of Industrial Mathematics, Germany, in the department of flow and material simulation. Pandurangan's current research includes monitoring and mapping of hydraulic fractures with far-field measurements and data-assimilation techniques. He holds a PhD degree in mechanical engineering from Nanyang Technological University, Singapore.

Anthony Peirce is a professor in the Department of Mathematics at the University of British Columbia, Canada. Previously, he worked as an applied mathematician at the Chamber of Mines Research Laboratories in South Africa, where he investigated rock-fracture processes around underground excavations. Peirce's research interests include the application of control to molecular systems, the analysis of instabilities in elasto-plastic materials, the development of specialized numerical algorithms to model large-scale rock-fracture processes, numerical and analytic studies of reactive flows in porous media, and, more recently, the asymptotic and numerical analysis of fluid-driven-fracture propagation. He has authored or coauthored more than 75 refereed papers. Peirce holds a PhD degree in applied and computational mathematics from Princeton University.

Zuorong Chen is a research scientist with CSIRO. Previously, he worked for the University of Sydney in the Department of Mechanical Engineering. Chen's current research interests include hydraulic-fracture monitoring and modeling, reservoir simulation, geomechanics, and the finite-element method. He holds a PhD degree in solid mechanics from Beijing University of Aeronautics and Astronautics. Chen is a member of SPE.

Rob Jeffrey is a senior geotechnical engineer with SCT Operations. Before July 2015, he worked with the hydraulic-fracturing team at CSIRO Energy. Jeffrey's research interests include hydraulic fracturing of naturally fractured rocks with applications in the petroleum, geothermal, and mining industries. He holds a PhD degree in geological engineering from the University of Arizona. Jeffrey is currently an associate editor for *SPE Journal*.